scientific reports

OPEN

Area-based breast percentage density estimation in mammograms using weight-adaptive multitask learning

Naga Raju Gudhe[1]✉, Hamid Behravan[1]✉, Mazen Sudah[2], Hidemi Okuma[2], Ritva Vanninen[2,3], Veli-Matti Kosma[1,4,5] & Arto Mannermaa[1,4,5]

Breast density, which is a measure of the relative amount of fibroglandular tissue within the breast area, is one of the most important breast cancer risk factors. Accurate segmentation of fibroglandular tissues and breast area is crucial for computing the breast density. Semiautomatic and fully automatic computer-aided design tools have been developed to estimate the percentage of breast density in mammograms. However, the available approaches are usually limited to specific mammogram views and are inadequate for complete delineation of the pectoral muscle. These tools also perform poorly in cases of data variability and often require an experienced radiologist to adjust the segmentation threshold for fibroglandular tissue within the breast area. This study proposes a new deep learning architecture that automatically estimates the area-based breast percentage density from mammograms using a weight-adaptive multitask learning approach. The proposed approach simultaneously segments the breast and dense tissues and further estimates the breast percentage density. We evaluate the performance of the proposed model in both segmentation and density estimation on an independent evaluation set of 7500 craniocaudal and mediolateral oblique-view mammograms from Kuopio University Hospital, Finland. The proposed multitask segmentation approach outperforms and achieves average relative improvements of 2.88% and 9.78% in terms of F-score compared to the multitask U-net and a fully convolutional neural network, respectively. The estimated breast density values using our approach strongly correlate with radiologists' assessments with a Pearson's correlation of $r = 0.90$ (95% confidence interval [0.89, 0.91]). We conclude that our approach greatly improves the segmentation accuracy of the breast area and dense tissues; thus, it can play a vital role in accurately computing the breast density. Our density estimation model considerably reduces the time and effort needed to estimate density values from mammograms by radiologists and therefore, decreases inter- and intra-reader variability.

Breast cancer (BC) occurs with the highest incidence of all cancers in women across 27 European Union countries (1,237,588 new cancer cases with 28.7% being BC; 555,650 total cancer deaths with 16.5% due to BC in 2020) (https://ecis.jrc.ec.europa.eu/). Early detection of BC is a critical diagnostic requirement for lowering the BC mortality rate. Digital X-ray mammography is the gold standard and the most reliable imaging technique for BC screening in the early stages. The European Reference Organization for Quality Assured Breast Screening and Diagnostic Services recommends regular breast screenings for women over the age of 40 for both craniocaudal (CC)-view and mediolateral oblique (MLO)-view mammograms[1].

Breast density has been identified as one of the strongest independent risk factors contributing to BC. Numerous studies demonstrated a positive association between breast density and BC risk[2–4]. The mammographic breast percentage density (PD) measures the relative amount of fibroglandular (also known as dense) tissue within the breast area. Women with higher PD values (> 75%) have an indicative risk of BC that is 4-to-6 fold higher than

[1]Institute of Clinical Medicine, Pathology and Forensic Medicine, Multidisciplinary Cancer Research community, University of Eastern Finland, P.O. Box 1627, 70211 Kuopio, Finland. [2]Department of Clinical Radiology, Kuopio University Hospital, P.O. Box 100, 70029 Kuopio, Finland. [3]Institute of Clinical Medicine, Radiology, Translational Cancer Research Area, University of Eastern Finland, P.O. Box 1627, 70211 Kuopio, Finland. [4]Biobank of Eastern Finland, Kuopio University Hospital, Kuopio, Finland. [5]These authors contributed equally: Veli-Matti Kosma and Arto Mannermaa. ✉email: raju.gudhe@uef.fi; hamid.behravan@uef.fi

women with lower PD values ($< 5\%$)[2]. The sensitivity of mammography is density dependent, i.e., the higher the density, the lower the sensitivity due to the masking effect[5]. The sensitivity is also affected by other factors, such as light intensity of the mammography machine, vendor specific processing protocol, perception errors, and the composition of the breast tissue[6]. In clinical practice, radiologists visually analyze the patterns and distribution of fibroglandular tissues within the mammograms and report the density scores following the Breast Imaging Reporting and Data System (BI-RADS)[7]. The 4th edition of BI-RADS categorizes the breast density into four quartiles in range of 0–100% with an increment of 25%. The assessment of breast density using BI-RADS 4th edition subjects to intra-reader variability[8]. To reduce this variability, the breast composition lexicon was updated in BI-RADS 5th edition. In the 5th edition, the qualitative analysis is replaced with subjectivity. With the highest incidence of BC, the need for the specialized radiologist is growing. Given shortage of expert radiologists and workload, substantial time and efforts are needed to examine mammograms at large scale. Moreover, the quantitative and qualitative assessments of the breast density by radiologists are subjective, leading to inter- and intra-reader variability[9].

There is a growing interest among medical imaging experts in developing fully automated methods that can assess PD values in a robust and quantifiable fashion. Semiautomated approaches, such as Cumulus[10] and DM-Scan[11], have been developed for area-based PD estimation. However, these approaches require the domain expert (radiologist) to adjust a threshold value to segment the dense tissues for each mammogram, leading to the same problems as with manual assessments: time needed, subjective results, and intra- and inter-reader variability. Fully automatic software, such as LIBRA[12] and Quantra[13], have been developed for area-based and volumetric-based PD estimation, respectively. Despite being leading-edge tools, LIBRA and Quantra have a few limitations, such as over- or under-segmenting the fibroglandular tissues[14]. In many instances, LIBRA performs poorly in delineating the pectoral muscle from the breast region[14], potentially due to data variability, different mammogram acquisition protocols, and vendor-specific post-processing techniques (in the case of processed mammograms). The pectoral muscle has similar pixel intensities and texture to the breast region, and the boundary separating the pectoral muscle and the breast region are usually obscure and irregular. Excluding the pectoral muscle from the breast region in MLO-view mammograms is another challenge that must be handled for accurate breast density estimation.

Traditional image processing techniques, such as thresholding[15] and clustering[16], have been well established for segmentation tasks. However, the major limitations of adopting traditional algorithms are selection of discriminative features in each given image for segmentation and finding an optimal threshold value to segment the fibroglandular tissues within the breast area. Artificial intelligence-based approaches, specifically deep learning (DL) algorithms based on convolutional neural networks (CNNs), have shown remarkable performances in various medical imaging applications[17–19]. The DL algorithms automatically extract the most descriptive and silent features within an image for a given task. The sophisticated computing infrastructure (graphical processing unit) enhances DL algorithms' training and deployment in the clinical settings. Long et al.[20] proposed an encoder–decoder-based fully convolutional neural networks (FCN) for the semantic segmentation task. The encoder captures the contextual and spatial information, and the decoder reconstructs the information and segments the regions of interest from the input mammogram. Inspired by this work[20], Ronneberger et al.[19] modified the FCN by introducing skip connections to concatenate features from the encoder to the corresponding decoder and named the architecture U-net. The gold-standard U-net architecture has been successfully incorporated in various biomedical image segmentation tasks. Despite its popularity, U-net has a few limitations, such as the loss of spatial information during concatenation of the features from the encoder to the decoder, and it often fails to segment regions of interest at different scales and variations[21,22].

Recently, multitask learning (MTL) was employed to improve the performance of image segmentation tasks[23–25]. Parameter sharing between subtasks is the most common approach used to perform MTL, as it avoids recomputing each task's parameters and thus improves computational speed by reducing memory usage[24]. MTL has been shown to have a higher generalization capability and to reduce overfitting[24,25]. Kendall et al.[23] proposed an MTL framework with multiple regression and classification tasks for semantic segmentation and demonstrated that task-dependent homoscedastic uncertainty improves the representation and individual task performance.

A few studies have incorporated DL algorithms into the breast-density estimation task using digital mammograms[26–30]. Kallengberg et al.[30] developed a sparse convolutional autoencoder to automatically extract features in a mammogram using an unsupervised learning technique. The learned features are fed to a simple neural network classifier for fatty- and dense-tissue classification[30]. They showed that the computed PD scores strongly correlate with the manual Cumulus scores ($r = 0.85$) and reported dice coefficients of 0.63 ± 0.19 and 0.95 ± 0.05 for the dense and fatty tissue segmentation. Lee et al.[14] developed a fully automatic DL algorithm for PD estimation based on the FCN approach that segments the breast area and dense tissues in the mammograms. The study considered BI-RADS[7] density ratings as ground truth and generated binary masks for the dense tissues. The PD values estimated by the algorithm showed Pearson correlation of $r = 0.81$ and $r = 0.79$ for the CC- and MLO-view mammograms, respectively, compared with those estimated using LIBRA. Other studies[26–29] used CNNs to classify the mammogram pixels into fatty and dense classes following BI-RADS 4th edition[31] .

Previous studies segmented the breast area using classical edge-detection techniques or contour-based methods[32]. These approaches often failed to delineate the pectoral muscle and air gaps within the mammogram[33]. Mammograms acquired from various sources and sites often differ in terms of pixel intensities. Segmenting the dense tissues using image histogram thresholding based on BI-RADS categories increases the sensitivity of the model[14]. Accurate segmentation of breast and dense tissues are vital to computing the PD values. The main contributions of this study are listed as follows:

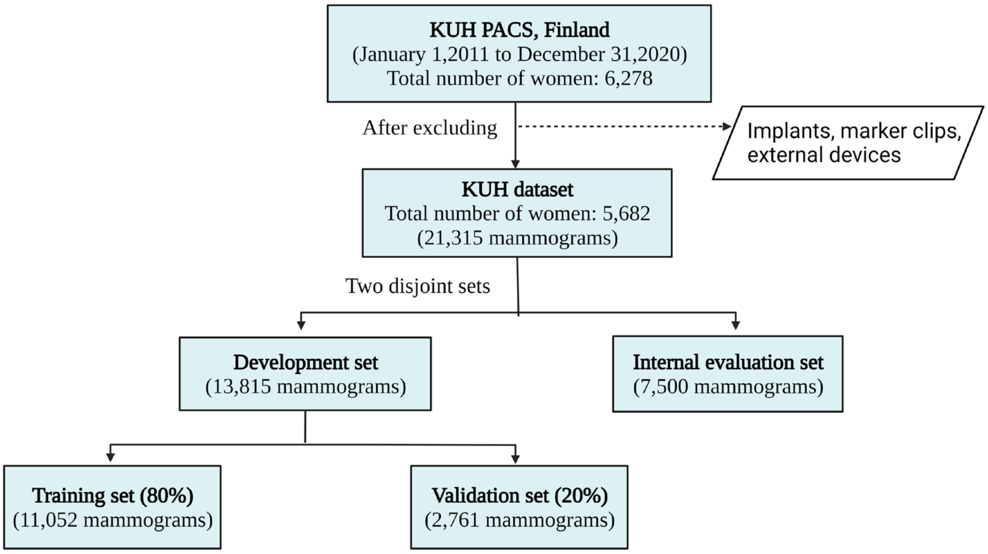

Figure 1. Flowchart describing the KUH dataset preparation. After excluding mammograms containing implants, marker clips, and/or external devices, we divided the KUH dataset into two disjoint sets: the development set and the internal evaluation set.

1. We proposed a multitask DL architecture, named MTLSegNet, that simultaneously segments the breast area and the dense tissues within a given mammogram and further computes the PD values using the segmented regions.
2. We generated 31,731 (21,315 from Kuopio University Hosptial (KUH) dataset and 10,416 from open-sourced datasets) breast-area and dense-tissue ground-truth binary masks for the segmentation task, under the supervision of two expert radiologists from KUH. The KUH data with annotations are available by request.
3. We evaluated the segmentation performance of the proposed approach against multitask U-net and FCN, as baseline approaches. We also compare the estimated PD values with existing LIBRA and Quantra software.

Material and methods

Data acquisition protocol.

The study was approved by the ethics committee of KUH. For the purposes of this retrospective image analysis, the need for patient consent was waived by the Chair of the Hospital District. All experiments were conducted according to the relevant guidelines and the principles expressed in the Declaration of Helsinki.

The KUH mammograms were acquired using Selenia Dimensions from Hologic, Inc. or AMULET Innovality from FUJIFILM corporation. The mammograms from the Kuopio region (Finland) were retrieved from the picture archiving and communications system. Pseudonymized digital mammograms (for Presentation) in DICOM format were collected from 6278 women from January 2011 to December 2020. Two expert radiologists with experience of 25 and 15 years reviewed all the mammograms, and any with a visual appearance of implants, marker clips, or device names, which considerably damage the breast region, were excluded. The resulting KUH dataset contains mammograms from 5682 women (21,315 mammograms).

Figure 1 shows the flowchart for preparing the KUH mammogram dataset. The KUH dataset was randomly divided into two disjoint sets, one for model development and the second for evaluating the model performance. The development set contained 13,815 mammograms and was further divided into a training set (80%; 11,052 mammograms) and validation set (20%; 2763 mammograms). The evaluation set contained 7500 mammograms and was used to demonstrate the performance of our proposed and baseline segmentation models, and to estimate the breast PD values. Note that the internal evaluation set is not used for the model development and training. To avoid data leakage, we ensured that mammograms from the same patients only appear in one set during the KUH data split.

To address the data variability problem, we also included three publicly available datasets: the Mammographic Image Analysis Society digital mammogram dataset (MIAS)[34], mini-DDSM[35], and INbreast[36]. The MIAS and mini-DDSM are open-source datasets, and for the INbreast dataset, we obtained written agreement from the authors for use in research. MIAS is the most requested dataset in the mammography research community. The original dataset was digitized with a 50-micron pixel edge. It consists of 322 digitized MLO-view mammograms from 161 women at 1024 × 1024 pixels, each with corresponding label information. The mini-DDSM is the lightweight version of the Digital Database for Screening Mammography (DDSM)[37], containing 9684 mammograms from 2421 women (mean age of 57.51 ± 12.71) with variable image dimensions between 125 and 320 pixels. INbreast is a full-field digital mammography dataset consisting of 410 mammograms from 115 women. The KUH data splitting protocol for the three publicly available datasets resulted in few test mammograms for model evaluation, especially in the MIAS and INbreast datasets. Therefore, we followed a 60:20:20 splitting protocol for training, validation, and evaluation for the MIAS, mini-DDSM, and INbreast datasets to maintain

	Development set				Evaluation set	
	Training set ($n = 17{,}304$)		Validation set ($n = 4845$)		Test set ($n = 9582$)	
Dataset	CC	MLO	CC	MLO	CC	MLO
KUH ($n = 21{,}315$)	5526	5526	1382	1381	3750	3750
MIAS ($n = 322$)	N. A	194	N. A	64	N. A	64
mini-DDSM ($n = 9684$)	2906	2906	968	968	968	968
INbreast ($n = 410$)	123	123	41	41	41	41

Table 1. The splitting protocol used in this study. We employed a 60:20:20 splitting protocol for training, validation, and evaluation sets for the MIAS, INbreast, and mini-DDSM datasets. Note that the splitting protocol for the KUH dataset is different than the public datasets. *N.A* not available.

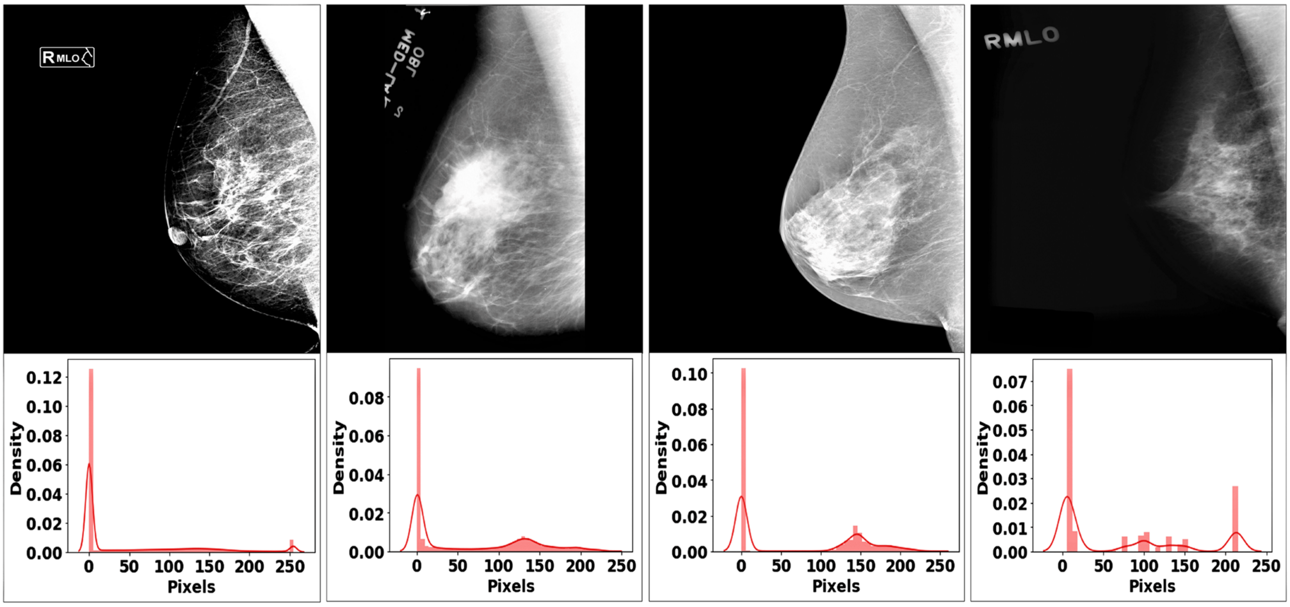

(a) (b) (c) (d)

Figure 2. Examples of mammograms from the datasets used in this study. (**a**) KUH, (**b**) MIAS, (**c**) INbreast, and (**d**) mini-DDSM. The histogram of the grayscale value distribution for each mammogram is given below the corresponding mammogram.

data distribution harmony and have a handful of mammograms to evaluate the performance of the proposed and the baseline approaches. Table 1 summarizes the datasets and the data splitting protocol used in this study. In total, we used 30% (9582) of the mammograms from the KUH and publicly available datasets for evaluation.

The datasets used in this study vary in the number of mammograms and the image pixel intensity distribution, as illustrated in Fig. 2. The variation could be potentially due to the vendor-specific processing of the mammograms and the acquisition protocols. We combined the datasets and normalized the mammograms using the normalizer technique[38] to develop a robust model capable of handling data variability issues. Normalization is a standard pre-processing technique that changes the range of pixel intensities of the individual image pixels and achieves consistency for the combined datasets.

Ground truth annotations and reference PD value computation. Under the guidance of two expert radiologists from KUH, we developed an in-house mammogram annotation tool and generated in total 31,731 breast-area and dense-tissue binary masks, among which 21,315 are from the KUH dataset and 10,416 from the publicly available datasets, used in this study. All the annotations were reviewed by an experienced BC radiologist from KUH.

Breast-area segmentation mask. The contour-based algorithms remove the background noise (labels, patient identification, visible markers) and segment the breast region[39]. Although contour-based approaches are simple and easy to use, breast-region segmentation is challenging, especially for the MLO-view mammograms, due to the similar intensity of the pectoral muscle and the breast region. Furthermore, the visual partition line between the pectoral tissue and the breast area is obscure and often irregular in shape. We manually segmented the breast area using the VGG Image Annotator software tool[40] and generated the annotations into JSON format, using OpenCV python package (https://docs.opencv.org/4.x/index.html), we generated the binary breast-area masks.

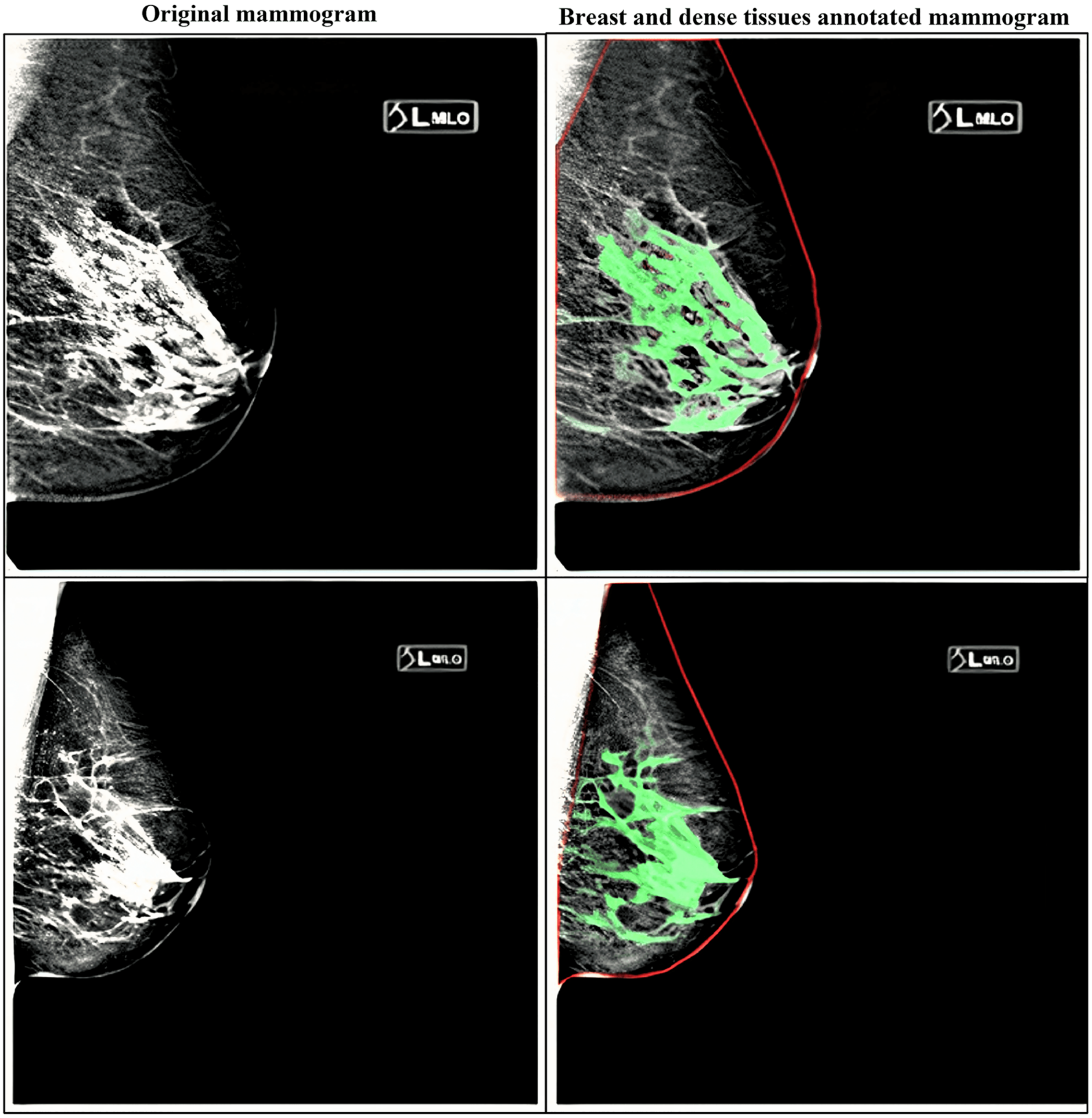

Figure 3. Examples of generated ground-truth segmentation masks from the KUH development set for the breast and dense-tissue segmentation. We overlapped the segmented binary masks on the original mammogram.

We used the generated breast-area mask and overlapped it with the original image to remove the background noise. All the background pixels were set to zero, and the intensity range of the breast area was normalized using the min-max normalization technique.

Dense-tissue segmentation mask. Based on BI-RADS categories, dense tissues are segmented using image-thresholding techniques[14]. With the variability in the image intensities and uncertainty in BI-RADS classification, the dense tissues are either over- or under-segmented. This study generated the dense-tissue binary masks using an in-house web-based interactive image segmentation tool developed in Python 3.6 and the Flask (https://flask.palletsprojects.com/en/2.0.x/) web framework under expert radiologist supervision. Figure 3 shows ground-truth annotations generated for the KUH dataset. The red contour line separates the breast area from other muscles, such as pectoral tissue in the MLO-view mammograms. The green pixels represent the dense (fibroglandular) tissues in the mammograms.

Reference PD value computation. For the KUH evaluation set (7,500 mammograms), two expert radiologists assessed the PD values, with an inter-reader correlation coefficient of 0.89. We have provided the Bland-Altman agreement plot between the two radiologists in Appendix A. We considered a difference of ± 5% PD value between the radiologists' given PD values, a clinically acceptable difference (CDI); 6840 out of 7,500 KUH evaluation mammograms are within the CDI. The estimated PD values by the two radiologists within the CDI range

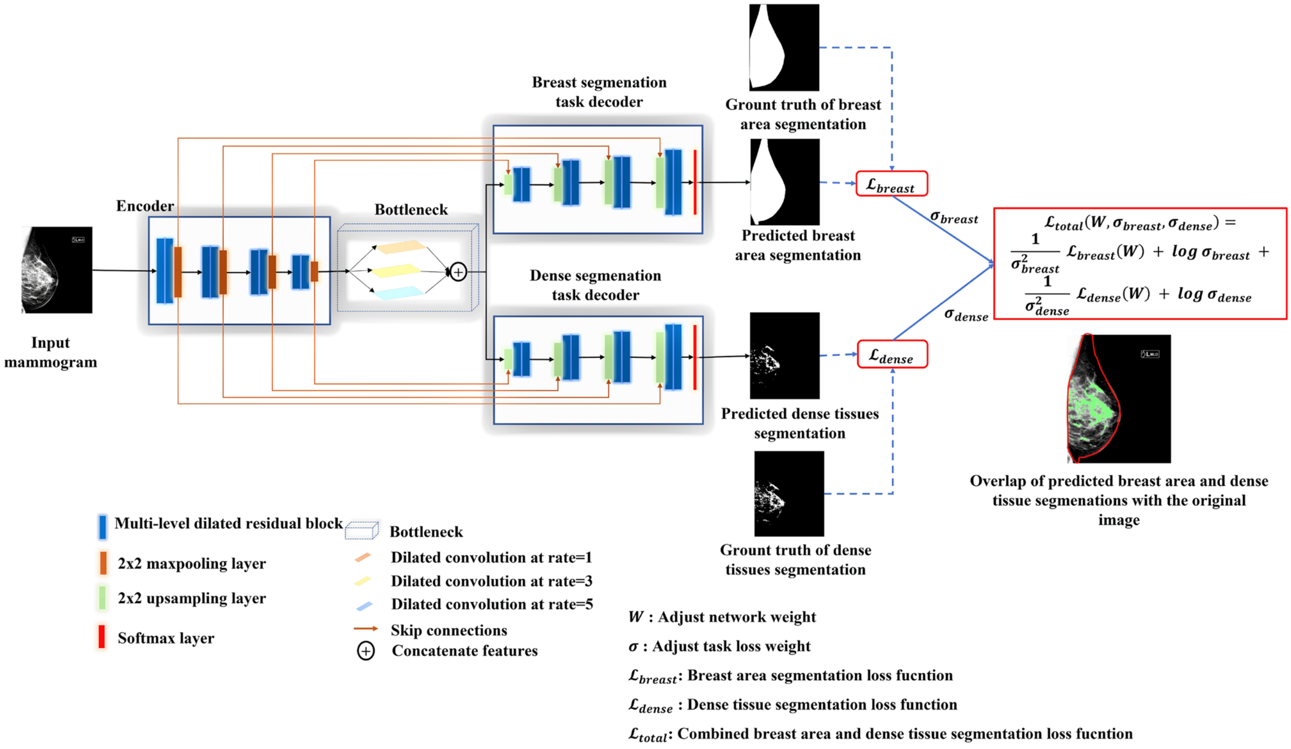
Breast segmenation task decoder
Grount truth of breast area segmentation
Encoder
Bottleneck
$\mathcal{L}_{breast}$
σ_{breast}
Predicted breast area segmentation
$\mathcal{L}_{total}(W, \sigma_{breast}, \sigma_{dense}) = \frac{1}{\sigma^2_{breast}} \mathcal{L}_{breast}(W) + log\ \sigma_{breast} + \frac{1}{\sigma^2_{dense}} \mathcal{L}_{dense}(W) + log\ \sigma_{dense}$
Input mammogram
Dense segmentation task decoder
σ_{dense}
$\mathcal{L}_{dense}$
Predicted dense tissues segmentation
Overlap of predicted breast area and dense tissue segmenations with the original image
Grount truth of dense tissues segmentation
Multi-level dilated residual block
2x2 maxpooling layer
2x2 upsampling layer
Softmax layer
Bottleneck
Dilated convolution at rate=1
Dilated convolution at rate=3
Dilated convolution at rate=5
Skip connections
Concatenate features
W : Adjust network weight
σ : Adjust task loss weight
$\mathcal{L}_{breast}$: Breast area segmentation loss fucntion
$\mathcal{L}_{dense}$: Dense tissue segmentation loss function
$\mathcal{L}_{total}$: Combined breast area and dense tissue segmentation loss fucntion

Figure 4. Illustration of the MTLSegNet architecture with encoder, bottleneck, and task-specific decoders. The encoder unit extracts the low- and high-level imaging features from the input mammogram. The extracted features are then fed into the bottleneck unit. The bottleneck unit further enhances the field of view by extracting more complex and spatial information at different resolutions. The task-specific decoders segment the breast area and the dense tissues, simultaneously. The loss function (focal Tversky loss[43]) is computed using the corresponding predicted and ground-truth segmentations of the breast area and the dense tissues. We modified the weight adaptive multi-task loss function[23] for the segmentation task and computed the combined loss of the breast-area and dense-tissue segmentation tasks. The predicted segmentation outputs are overlapped with the original mammogram. The red contour line is the predicted segmented breast area, and the solid green pixels represent the predicted fibroglandular tissues within the breast area.

were then averaged and used as a reference PD value for a given mammogram. For LIBRA and Quantra, we computed the PD values using LIBRA software tool version 1.0.4 and Selenia Dimensions®, Hologic Inc., Bedford machine equipped with Quantra tool, respectively.

Proposed architecture. An overview of the proposed MTLSegNet architecture is illustrated in Fig. 4. MTLSegNet is based on the MTL approach with two task-specific networks to segment the breast area and the dense tissue simultaneously. We considered the dense-tissue segmentation as the main task and the breast-area segmentation as the auxiliary task. This helps the model better differentiate the breast area from other tissues, such as pectoral and abdominal tissue, in the MLO-view mammograms and enhances the dense-tissue segmentation within the breast area. The task-specific decoders share parameters with the encoder network, and the depth of the encoder network is similar to that of the U-net encoder network. We replaced the conventional blocks in the encoder and decoder paths with multilevel dilated residual blocks, as suggested in Gudhe et al.[22], to enhance the learning capabilities of the network.

Additionally, we introduced three parallel dilated convolutions[41] with dilation rates of $d = 1$, 3, and 5 as a bottleneck that expands the field of view by extracting more complex and spatial information at different resolutions. The decoder part of each task has up-sampling layers with transpose convolutions. The extracted features from the encoder are concatenated with the corresponding decoder layer, and the nonlinear residual skip connections restore the information loss during the transition of up-sampling features to down-sampling in the decoder[22]. The prediction layer of the individual tasks is a 1×1 convolution layer activated by SoftMax[42] as a nonlinear function that predicts the probability maps of the breast area and the dense tissues. We modified the weighted multitask loss function[23] to compute the combined loss of the breast-area and the dense-tissue segmentation tasks.

Weight-adaptive multitask learning. Multitask learning is an inductive-transfer learning approach that improves generalization by sharing domain information among multiple tasks[23–25]. MTLSegNet consists of a common encoder and two decoders for the breast-area and dense-tissue segmentation. The features extracted from the encoder are shared by the two independent tasks.

Consider a dataset $\mathrm{D} = \{(x^{(i)}, y_b^{(i)}, y_d^{(i)})\}_{i=1}^{M}$, where $x^{(i)}$ represents the input mammogram of the instance i, and $y_b^{(i)}$ and $y_d^{(i)}$ are the breast-area and the dense-tissue ground-truth binary masks of the corresponding instance i. The learning function F of the MTL approach is represented as $\mathrm{F}(x^{(i)}, \theta_b^{(i)}, \theta_d^{(i)})$, where $\theta_b^{(i)}$ and $\theta_d^{(i)}$ are the network's weight parameters for the independent breast-area and dense-tissue segmentation tasks, respectively. The total energy function $\mathbf{E}_{\text{total}}$ is defined as follows:

$$\mathbf{E}_{\text{total}} = \lambda_b \mathbf{E}_b(\theta_b) + \lambda_d \mathbf{E}_d(\theta_d) \tag{1}$$

where $\mathbf{E}_b$ and $\mathbf{E}_d$ are the energy functions, and λ_b and λ_d are non-negative hyperparameters with arbitrary values between (0,1]. Generally, the values of λ_b and λ_d are manually chosen until the model generalization is optimized, the so-called naïve approach. The parameter selection for the naïve approach is difficult and involves considerable computation, while the trained model usually becomes biased toward a specific task[23].

The naïve multitask loss function is defined as follows[23]:

$$\mathbf{L}_{\text{total}}(\mathrm{D} : \theta_b, \theta_d) = \lambda_b \times \mathbf{L}_b(\mathrm{D} : \theta_b) + \lambda_d \times \mathbf{L}_d(\mathrm{D} : \theta_d). \tag{2}$$

Since the λ_b and λ_d values are in the range (0, 1] and $\lambda_b + \lambda_d \leq 1$, for simplicity, Equation (2) can be rewritten as:

$$\mathbf{L}_{\text{total}}(\mathrm{D} : \theta_b, \theta_d) = \lambda \times \mathbf{L}_b(\mathrm{D} : \theta_b) + (1 - \lambda) \times \mathbf{L}_d(\mathrm{D} : \theta_d). \tag{3}$$

Motivated by[23,44] , we modified the weight uncertainty loss function for segmenting the breast area and the dense tissues. The relative task weights, λ_b and λ_d, are learned by considering the uncertainty in the output predictions of each individual task. We define the weight-adaptive multitask loss function $\mathbf{L}_{total}$ as follows:

$$\mathbf{L}_{\text{total}}(\mathrm{D} : \theta, \sigma_b, \sigma_d) = \mathbf{L}_b(\mathrm{D} : \theta, \sigma_b) + \mathbf{L}_d(\mathrm{D} : \theta, \sigma_d) \tag{4}$$

where $\mathbf{L}_b$ and $\mathbf{L}_d$ are the loss functions for the breast-area and dense-tissue segmentations, with σ_b and σ_d as the corresponding task weights for λ_b and λ_d, respectively. Consider the likelihood of the model for each segmentation task as a scaled version of the model output $\mathrm{f}^{\theta}(x)$ with uncertainty σ, and θ as a network weight parameter squashed through a SoftMax function:

$$p(y|\mathrm{f}^{\theta}(x), \sigma) = \text{softmax}\left(\frac{1}{\sigma^2}\mathrm{f}^{\theta}(x)\right). \tag{5}$$

Using the negative log-likelihood, the segmentation loss with uncertainty is expressed as follows:

$$\log p(y = c|\mathrm{f}^{\theta}(x), \sigma) = \frac{1}{\sigma^2}\mathrm{f}^{\theta}(x) - \log\, \Sigma_{c'} \exp\left(\frac{1}{\sigma^2}\mathrm{f}_{c'}^{\theta}(x)\right) \tag{6}$$

where $\mathrm{f}_{c'}^{\theta}(x)$ is the cth element of the vector $\mathrm{f}^{\theta}(x)$.

The multitask loss function $\mathbf{L}_{\text{total}}(\theta, \sigma_b, \sigma_d)$ is defined as:

$$\begin{aligned} \mathbf{L}_{\text{total}}(\theta, \sigma_b, \sigma_d) &= -\log p(y_b, y_d = c|\, \mathrm{f}^{\theta}(x)) \\ &= \log p(y_b = c;\, \mathrm{f}^{\theta}(x), \sigma_b) + \log p(y_d = c;\, \mathrm{f}^{\theta}(x), \sigma_d) \\ &= \frac{1}{\sigma_b^2} - \log\, \Sigma_{c'} \exp\left(\frac{1}{\sigma_b^2}\mathrm{f}_{c'}^{\theta}(x)\right) + \frac{1}{\sigma_d^2} - \log\, \Sigma_{c'} \exp\left(\frac{1}{\sigma_d^2}\mathrm{f}_{c'}^{\theta}(x)\right) \\ &\approx \frac{1}{\sigma_b^2}\mathbf{L}_b(\theta) + \log\sigma_b + \frac{1}{\sigma_d^2}\mathbf{L}_d(\theta) + \log\sigma_d. \end{aligned} \tag{7}$$

We employed the focal Tversky loss function (FTL)[43] for each individual task, $\mathbf{L}_b$ and $\mathbf{L}_d$.

For each pixel j, $y_b^{(j)}$ and $y_d^{(j)}$ are the ground truths for the breast area and dense tissue, respectively, and $\hat{y}_b^{(j)}$ and $\hat{y}_d^{(j)}$ are the corresponding predicted segmentation masks. The FTLs for the breast-area and dense-tissue segmentation tasks are then defined as follows:

$$\mathbf{L}_b = \Sigma_c \left(1 - \left(\frac{\Sigma_{j=1}^{N} \hat{y}_b^{(j)c}\; y_b^{(j)c} + \varphi}{\Sigma_{j=1}^{N} \hat{y}_b^{(j)c}\; y_b^{(j)c} + \alpha\; \Sigma_{j=1}^{N} \hat{y}_b^{(j)\bar{c}}\; y_b^{(j)c} + \beta\; \Sigma_{j=1}^{N} \hat{y}_b^{(j)c}\; y_b^{(j)\bar{c}} + \varphi}\right)\right)^{\frac{1}{\gamma}} \tag{8}$$

$$\mathbf{L}_d = \Sigma_c \left(1 - \left(\frac{\Sigma_{j=1}^{N} \hat{y}_d^{(j)c}\; y_d^{(j)c} + \varphi}{\Sigma_{j=1}^{N} \hat{y}_d^{(j)c}\; y_d^{(j)c} + \alpha\; \Sigma_{j=1}^{N} \hat{y}_d^{(j)\bar{c}}\; y_d^{(j)c} + \beta\; \Sigma_{j=1}^{N} \hat{y}_d^{(j)c}\; y_d^{(j)\bar{c}} + \varphi}\right)\right)^{\frac{1}{\gamma}} \tag{9}$$

where c and $\bar{c}$ denote two class labels for region of interest and background, respectively. The total number of pixels in an image is denoted by $N$and φ prevents division by zero. The hyperparameters α and β can be tuned to improve the recall in case of class imbalance. The hyperparameter γ represents the focal parameter for detecting hard classes with lower probabilities. We used $\alpha = 0.3$, $\beta = 0.7$, and $\gamma = 1$ as penalties, as suggested in[43].

Computing area-based percentage mammogram density. The outputs of MTLSegNet are the probability scores of the breast-area and dense-tissue segmentations. We applied a threshold of 0.5 to convert the probability scores into binary masks. We resized the output predictions to their original image dimensions, as the reconstructed spatial resolutions are less than the original image spatial resolution due to the down-sampling and up-sampling operations. The PD value is computed as follows:

$$PD = \frac{\Sigma_{j=1}^{N}\, \hat{y}_d^{(j)}}{\Sigma_{j=1}^{N}\, \hat{y}_b^{(j)}} \times 100 \tag{10}$$

where $\hat{y_b}$ and $\hat{y_d}$ are the predicted breast-area and dense-tissue segmentation binary masks containing the white pixels only.

Implementation, evaluation metrics, and statistical analysis

Implementation details. We implemented the proposed and the baseline approaches, multitask U-net and FCN, in Python 3.6 using PyTorch 1.3.1[45], as the DL framework. Additionally, we implemented Otsu thresholding[46], as a conventional approach, to segment fibroglandular tissues. We considered four steps to estimate PD value of a given mammogram using Otsu thresholding: first, we generated the segmented breast area following the protocol described in "Ground truth annotations and reference PD value computation" *Breast-area segmentation mask* and converted the segmented breast area into a grayscale image. In second step, we smoothened the grayscale segmented breast area using a Gaussian blur with a kernel size of 5. Then, we applied Otsu thresholding to segment the fibroglandular tissues. Finally, using Eq. (10), we computed the PD value.

The datasets considered in this study were acquired from different devices, introducing variability to the image dimensions, intensity, and visual appearance. We resized all the images to 256 × 256 dimensions using bicubic interpolation to maintain the original aspect ratio. We combined all the validation set of mammograms from all datasets and fine-tuned the proposed model to find the optimal hyperparameters, including optimizer, learning rate, learning rate schedulers, and loss functions. We implemented the Bayesian optimization technique[47] using an adaptive experimentation platform[48] to find the optimal hyperparameters for the proposed model, the experiment results are provided in Appendix B. Additionally, we investigated the impact of various normalization techniques, including batch normalization[49], instance normalization[50], group normalization[51], and weight standard normalization[52], at batch sizes of 2, 4, 8, and 16 on the performance of the multitask segmentation models using the validation set of all the datasets. The normalization techniques accelerate the training process of DL models and help them converge faster[49]. The batch size and normalization experiment results are presented in Appendix C.

The proposed MTLSegNet and the baseline approaches were trained using the optimal hyperparameters for 100 epochs on a machine equipped with an Nvidia Tesla V100 16GB graphic card on an Intel Xeon processor provided by the IT Service Centre for Science (CSC) Finland[53]. The implementation source codes are available at https://gitlab.com/rajgudhe.uef/mtlsegnet.

Segmentation evaluation metrics. We evaluated the segmentation performance of MTLSegNet and the baseline models using F-score and intersection over union (IoU). For a given image x, let y and $\hat{y}$ be the ground-truth and predicted binary masks, respectively. The evaluation metrics are defined as follows:

$$\text{Precision} = \frac{\Sigma_{j=1}^{N}\, \hat{y}^{(j)} \cap y^{(j)}}{\Sigma_{j=1}^{N} \hat{y}^{(j)}} \tag{11}$$

$$\text{Recall} = \frac{\Sigma_{j=1}^{N}\, \hat{y}^{(j)} \cap y^{(j)}}{\Sigma_{j=1}^{N} y^{(j)}} \tag{12}$$

$$\text{F} - \text{score} = \frac{2 \times \text{Precision} \times \text{Recall}}{\text{Precision} + \text{Recall}} \tag{13}$$

$$\text{IoU} = \frac{\Sigma_{j=1}^{N}\, \hat{y}^{(j)} \cap y^{(j)}}{\Sigma_{j=1}^{N}\, \hat{y}^{(j)} \cup y^{(j)}} \tag{14}$$

Statistical evaluation of the estimated breast-density values. To determine the degree of association between the estimated PD values of MTLSegNet and baseline models with the radiologists provided reference PD values, Pearson's correlation coefficients[54] r at 95% confidence intervals (CI) were computed for each mammogram view. Bland–Altman plots[55] was used to measure the limits of agreement (LoA) between the density estimation models at 95% CI.

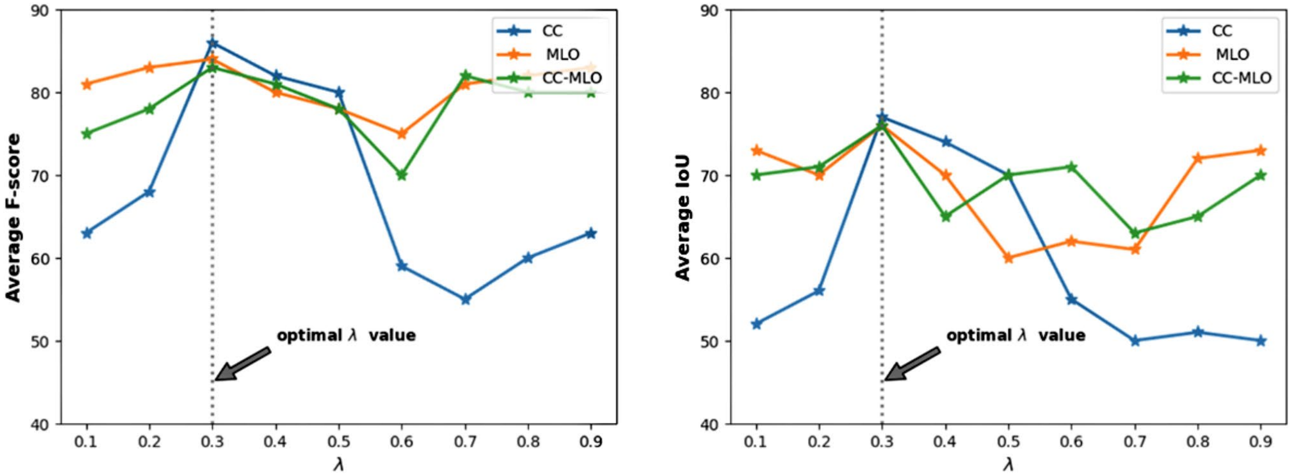

Figure 5. The performance of the naïve multitask loss function on the combined validation set. The weight parameter λ in the range 0.1–0.9 is on the x-axis, and the segmentation evaluation metrics, IoU and F-score, are on the y-axis. The segmentation model trained with $\lambda = 0.3$ shows better performance compared to the other λ values.

	Naïve multitask		Weight-adaptive multitask	
Combined validation set ($n = 4845$)	**F-score**	**IoU**	**F-score**	**IoU**
CC ($n = 2391$)	85.2	76.9	**85.9**	**78.3**
MLO ($n = 2454$)	83.5	75.2	**91.1**	**84.2**
CC-MLO ($n = 4845$)	83.7	75.2	**92.2**	**85.9**

Table 2. The comparison of naïve multitask loss function with the modified weight-adaptive multitask loss function. The model trained with weight-adaptive multitask loss function shows superior performance in segmenting the breast area and the dense tissues than the naïve approach, with relative improvements of 10.15% and 14.23% in terms of F-score and IoU, respectively, on the CC-MLO-view mammograms of the combined validation sets. Best values are in [bold].

Results

In this section, we demonstrate the quantitative and qualitative performance of MTLSegNet for both segmentation and PD value estimation. For the breast-area and dense-tissue segmentations, we compare the performance of MTLSegNet against the baseline approaches, FCN and U-net. Furthermore, we compare the accuracy of the MTLSegNet-estimated PD values with the radiologist-provided, LIBRA-computed, and Quantra-computed PD values. Model evaluation is given for both CC- and MLO-views and the combined CC-MLO view mammograms. The CC-MLO view is formed by randomly shuffling the CC- and MLO-view mammograms from the evaluation sets of all datasets. We then combined the CC- and MLO-view mammograms from the same patients and created the CC-MLO-view evaluation set.

Performance of breast and dense-tissue segmentation using MTLSegNet and baseline approaches.

Weight-adaptive multitask learning outperforms the naïve multitask learning approach. In this section, we demonstrate the efficacy of the weight-adaptive MTL, Eq. (7), compared to the naïve MTL, Eq. (3). For the naïve MTL, we implemented the trial-and-error approach, with λ values in the range (0,1). Figure 5 shows the segmentation accuracy of different values of λ in terms of F-score and IoU on the combined validation sets. The model trained with $\lambda = 0.3$ shows a better average segmentation performance for the CC-, MLO-, and CC-MLO-view mammograms.

The naïve multitask approach is an expensive grid search and time-consuming approach to find the optimal value of λ. We compared the performance of the modified weight-adaptive multitask loss function with the optimal weight parameter $\lambda = 0.3$ of the naïve multitask loss function. Table 2 shows that the modified weight-adaptive loss function performs better in segmenting the breast area and the dense tissues than the naïve approach for the CC-MLO-view of the combined datasets, with relative improvements of 10.15% and 14.23% in terms of F-score and IoU, respectively. The advantage of using the weight-adaptive multitask loss function is that the model automatically estimates the weight parameters by considering the weighted uncertainty parameter σ of both the breast-area and the dense-tissue segmentations, which is considerably computationally less inexpensive than the naïve approach. It also reduces the bias between the primary task (dense-tissue segmentation) and the auxiliary task (breast-area segmentation).

Combined validation set (*n* = 4845)			**Single task**		**Multitask**	
Model	**Tissue**	**view**	**F-score**	**IoU**	**F-score**	**IoU**
FCN	Breast	**CC** (*n* = **2391)**	83.15 ± 0.013	73.16 ± 0.001	80.31 ± 0.037	70.19 ± 0.003
		MLO(*n* = **2454**)	82.68 ± 0.001	70.38 ± 0.003	76.51 ± 0.003	72.72 ± 0.001
		CC-MLO (*n* = **4845**)	80.16 ± 0.019	63.16 ± 0.003	79.36 ± 0.003	70.32 ± 0.003
	Dense	**CC** (*n* = **2391**)	68.39 ± 0.02	58.16 ± 0.015	70.16 ± 0.016	68.26 ± 0.12
		MLO (*n* = **2454**)	65.62 ± 0.001	57.82 ± 0.013	73.19 ± 0.032	67.37 ± 0.220
		CC-MLO (***n* = *4845***)	***65.13 ± 0.002***	***57.10 ± 0.0012***	***73.03 ± 0.16***	***67.03 ± 0.11***
U-net	Breast	**CC** (*n* = **2391**)	87.32 ± 0.011	87.13 ± 0.003	84.19 ± 0.002	74.16 ± 0.009
		MLO (*n* = **2454**)	86.31 ± 0.003	86.09 ± 0.003	84.73 ± 0.005	72.78 ± 0.0042
		CC-MLO(*n* = **4845)**	87.51 ± 0.003	83.32 ± 0.001	85.13 ± 0.005	71.56 ± 0.019
	Dense	**CC** (*n* = **2391**)	71.53 ± 0.002	62.15 ± 0.013	73.36 ± 0.113	72.61 ± 0.001
		MLO (*n* = **2454**)	70.31 ± 0.002	61.92 ± 0.03	71.58 ± 0.056	70.32 ± 0.063
		CC-MLO (*n* = ***4845)***	***68.19 ± 0.003***	***56.12 ± 0.017***	***70.19 ± 0.005***	***68.13 ± 0.007***
MTLSegNet	Breast	**CC** (*n* = **2391)**	89.181 ± 0.003	88.381 ± 0.006	85.840 ± 0.001	82.286 ± 0.001
		MLO (*n* = **2454)**	89.098 ± 0.004	88.223 ± 0.009	88.906 ± 0.008	87.852 ± 0.016
		CC-MLO (*n* = **4845**)	89.095 ± 0.003	88.212 ± 0.007	88.940 ± 0.007	87.915 ± 0.013
	Dense	**CC** (*n* = **2391)**	73.651 ± 0.03	68.899 ± 0.038	81.866 ± 0.013	75.041 ± 0.021
		MLO (*n* = **2454)**	70.195 ± 0.037	64.690 ± 0.035	81.965 ± 0.014	75.202 ± 0.022
		CC-MLO (*n* = ***4845)***	***72.278 ± 0.022***	***67.140 ± 0.023***	***82.042 ± 0.010***	***75.323 ± 0.016***

Table 3. The multitask learning approach shows superior segmentation performance compared to the single-task approach. For the multitask learning approach, we computed the evaluation metrics independently on the predictions of the two task-specific decoders. We compared the dense-tissue segmentation of CC-MLO-view mammograms for both the single-task and multitask approaches of FCN, U-net, and MTLSegNet (highlighted in bolditalics). Best values are in [bold].

Multitask learning shows superior performance compared to single-task segmentation. We trained MTLSegNet and the baseline methods for both single-task and multitask segmentations. For the single-task segmentation, we removed the second decoder from the architectures and trained all models with the optimal hyperparameters (more details are enclosed in Appendix B) for 100 epochs. We compared the performance of the individual tasks, the breast-area and the dense-tissue segmentations, against the multitask learning approach using the combined validation sets. For the multitask learning, we computed the evaluation metrics independently for the two task-specific decoders.

Table 3 shows that the proposed multitask MTLSegNet approach outperforms the single-task approach in segmenting dense tissues by average relative improvement of 13.5% in terms of F-score on the CC-MLO-view mammograms. For the single-task approach, MTLSegNet outperforms the FCN and U-net dense-tissue segmentations by relative improvements of 10.97% and 5.99% in terms of F-score, respectively. Regarding the multitask approach, MTLSegNet shows superior performance for the dense-tissue segmentation compared to the multitask FCN and U-net by relative improvements of 12.34% and 16.88% in terms of F-score, respectively. We also notice that the breast-area segmentation by the single-task model performs slightly better than the multitask approach. Note that in the multitask segmentation approach, the model simultaneously segments the breast area and the dense tissues. To reduce the bias between the two tasks, the weight parameter of the individual decoder networks is balanced by the weight-adaptive loss function. In the single-task approach, the loss function is generalized to a specific task (e.g., the breast-area segmentation), thus achieving slightly better accuracy.

MTLSegNet outperforms the multitask segmentation U-net and FCN models. Table 4 shows that the proposed MTLSegNet approach outperforms the Otsu, FCN and U-net networks in all datasets. Average relative improvements of 24.07%, 3.17% and 2.29% in terms of F-score are observed over the Otsu, FCN and U-net, respectively, in the combined CC-MLO-view evaluation set of all datasets. The highest segmentation improvements with MTLSegNet over the DL approaches are attributed to the CC-MLO-view images of the KUH evaluation data, at 9.78% and 2.88% relative improvements over the FCN and U-net networks, respectively. Similarly, the lowest segmentation improvements with MTLSegNet are attributed to the CC-view of the mini-DDSM dataset, at 1.08% and 0.11% relative improvements over the FCN and U-net networks, respectively.

Figures 6 and 7 show a few segmentation outputs predicted by the MTLSegNet, U-net, and FCN networks on the KUH evaluation data. For the CC-view mammograms, the breast-area segmentation accuracy for all models is similar (Fig. 6 , first row). For the MLO-view mammograms, MTLSegNet successfully delineated the breast area from other tissues, such as abdominal tissues, as shown in red contours in the second row of Fig. 6.

Figure 7 shows that, for both CC- and MLO-view images, the MTLSegNet model precisely segments the dense tissues by ignoring the fat tissues within the breast area, while the U-net and FCN models included the fat tissues, resulting in over-segmentation. The introduction of dilated convolutions as a bottleneck in the MTLSegNet architecture has potentially improved the dense-tissue segmentation compared to FCN and U-net.

Evaluation set ($n = 9582$)	View	Model	F-score	IoU
KUH ($n = 7500$)	CC	Otsu	55.32 ± 0.31	47.51 ± 0.03
		FCN	71.56 ± 0.11	60.21 ± 0.13
		U-net	80.09 ± 0.07	70.48 ± 0.08
		MTLSegNet	**81.27 ± 0.06**	**71.95 ± 0.07**
	MLO	Otsu	62.56 ± 0.03	51.36 ± 0.05
		FCN	75.91 ± 0.05	65.41 ± 0.06
		U-net	79.65 ± 0.05	69.59 ± 0.06
		MTLSegNet	**80.41 ± 0.04**	**70.83 ± 0.05**
	CC-MLO	Otsu	68.16 ± 0.02	57.39 ± 0.07
		FCN	75.32 ± 0.06	65.76 ± 0.21
		U-net	80.37 ± 0.13	70.53 ± 0.22
		MTLSegNet	**82.69 ± 0.02**	**73.40 ± 0.02**
MIAS ($n = 64$)	MLO	Otsu	44.37 ± 0.02	51.56 ± 0.11
		FCN	75.51 ± 0.14	65.10 ± 0.14
		U-net	78.28 ± 0.10	67.77 ± 0.10
		MTLSegNet	**78.75 ± 0.13**	**68.41 ± 0.13**
mini-DDSM ($n = 1936$)	CC	Otsu	69.72± 0.03	76.32± 0.01
		FCN	92.09 ± 0.00	85.82 ± 0.01
		U-net	92.98 ± 0.01	87.27 ± 0.02
		MTLSegNet	**93.09 ± 0.01**	**87.43 ± 0.02**
	MLO	Otsu	31.52 ± 0.06	57.56 ± 0.02
		FCN	75.51 ± 0.14	65.10 ± 0.14
		U-net	78.28 ± 0.10	67.77 ± 0.10
		MTLSegNet	**78.75 ± 0.13**	**68.41 ± 0.13**
	CC-MLO	Otsu	75.32 ± 0.04	71.56 ± 0.05
		FCN	91.78 ± 0.00	85.23 ± 0.01
		U-net	92.70 ± 0.01	86.71 ± 0.02
		MTLSegNet	**92.83 ± 0.01**	**86.92 ± 0.02**
INbreast ($n = 82$)	CC	Otsu	58.16 ± 0.13	45.31 ± 0.05
		FCN	65.93 ± 0.14	58.77± 0.12
		U-net	70.87 ± 0.08	62.85 ± 0.07
		MTLSegNet	**72.13 ± 0.09**	**63.99 ± 0.08**
	MLO	Otsu	55.36 ± 0.12	40.5 ± 0.12
		FCN	67.23 ± 0.14	57.65 ± 0.13
		U-net	67.50 ± 0.13	57.79 ± 0.12
		MTLSegNet	**68.41 ± 0.09**	**58.88 ± 0.08**
	CC-MLO	Otsu	59.32 ± 0.05	48.16 ± 0.11
		FCN	73.69 ± 0.10	64.39 ± 0.09
		U-net	75.17 ± 0.08	65.97 ± 0.07
		MTLSegNet	**75.54 ± 0.07**	**66.55 ± 0.06**
Combined evaluation set ($n = 9582$)	CC	Otsu	71.56 ± 0.01	68.32 ± 0.02
		FCN	81.60 ± 0.14	74.38 ± 0.14
		U-net	83.32 ± 0.12	75.71 ± 0.13
		MTLSegNet	**85.92 ± 0.10**	**78.35 ± 0.11**
	MLO	Otsu	67.56 ± 0..5	54.16 ± 0.32
		FCN	89.87 ± 0.02	82.35 ± 0.02
		U-net	90.49 ± 0.02	83.32 ± 0.03
		MTLSegNet	**91.14 ± 0.02**	**84.28 ± 0.03**
	CC-MLO	Otsu	74.31 ± 0.01	70.30 ± 0.12
		FCN	89.36 ± 0.91	82.47 ± 0.22
		U-net	90.13 ± 0.11	84.29 ± 0.17
		MTLSegNet	**92.20 ± 0.01**	**85.99 ± 0.02**

Table 4. The proposed MTLSegNet segmentation approach outperforms the FCN and U-net networks in all datasets. Numbers in parentheses denote the number of evaluation data points in each dataset. We compare the performance of MTLSegNet on the individual validation datasets for CC-, MLO-, and CC-MLO-view mammograms in terms of F-score and IoU, as evaluation metrics. Best values are in [bold].

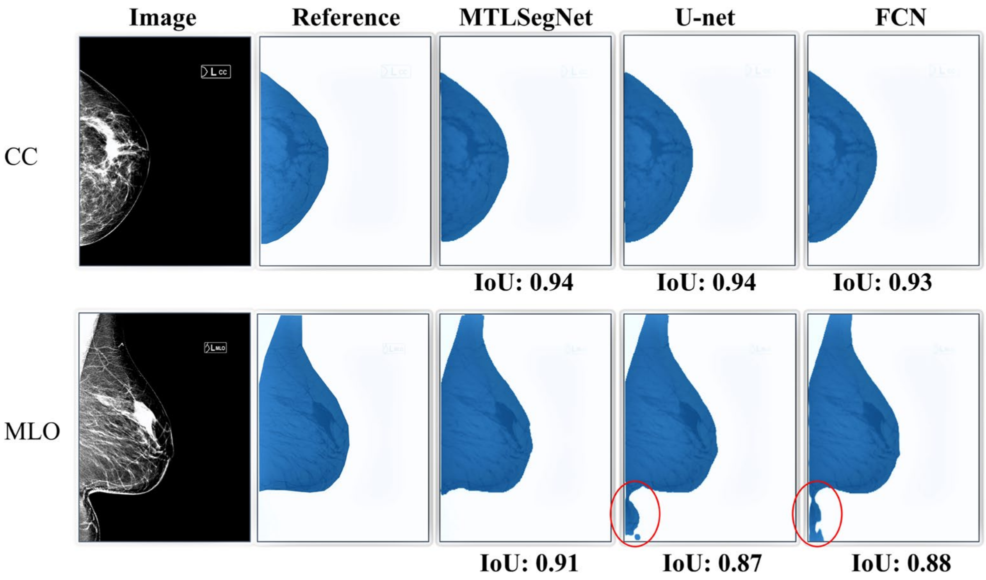

Figure 6. Breast-area segmentation outputs predicted by the MTLSegNet, U-net, and FCN networks on the KUH evaluation data. Red contours point to segmented regions of other tissue (in this case, abdominal tissues) predicted by the U-net and FCN models in the MLO-view.

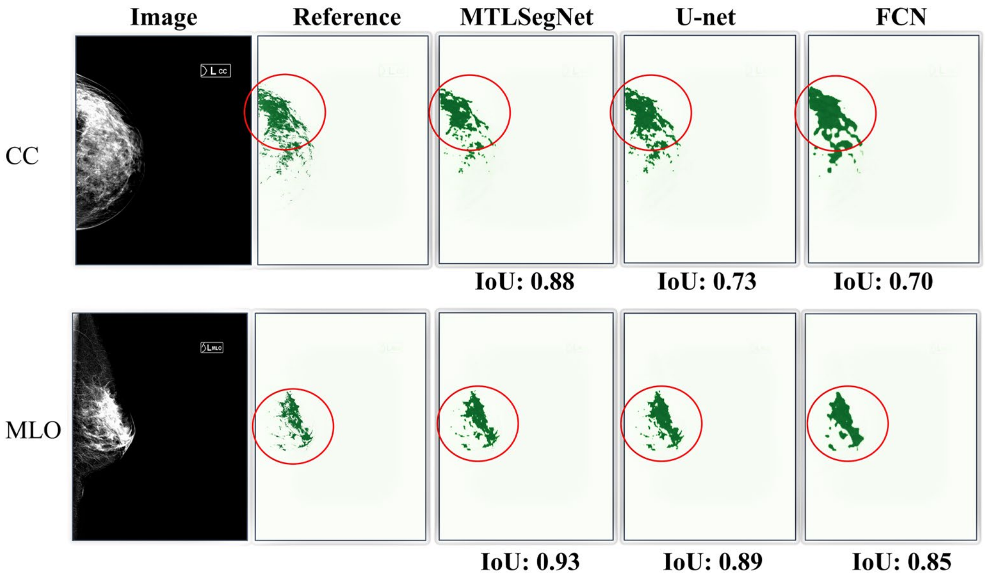

Figure 7. Dense-tissue segmentation outputs predicted by the MTLSegNet, U-net, and FCN networks on the KUH evaluation data. MTLSegNet successfully segmented the dense tissues, while FCN and U-net over-segmented the dense tissues by including the fat tissues within the breast area. For the visualization purposes, we outline the dense-tissue pixel area using the red contour.

More segmentation examples for qualitative assessment of the MTLSegNet approach are provided in Appendix D.

Area-based breast percentage density estimation:. *MTLSegNet more accurately estimates the breast density values compared to the baseline DL approaches.* The descriptive statistical summary of the estimated PD values by the baseline models is shown in Table 5. The mean difference between the FCN, and U-net PD values and the radiologist-provided PD values were 0.19%, and 1.9%, respectively, in the CC-MLO-view mammograms. For the KUH evaluation dataset, the average mean difference between MTLSegNet estimated PD values and the reference PD values are similar with a Pearson correlation of $r = 0.90$ (p value < 0.001). In the CC-view mammograms of KUH evaluation dataset, the FCN estimated PD values are close to the radiologist assessment. The U-net model overestimated the PD values for both CC- and CC-MLO-view mammograms compared with

KUH evaluation set ($n = 6840$)			
View	**PD estimation**	**Mean ± SD**	**$PD_{model} - PD_{radiologist}$**
CC ($n = \mathbf{3,528}$)	Radiologist	10.38 ± 5.77	–
	FCN	$\mathbf{10.45} \pm \mathbf{4.85}$	0.07
	U-net	14.17 ± 6.47	3.79
	MTLSegNet	11.28 ± 5.75	0.9
MLO ($n = \mathbf{3,312}$)	Radiologist	8.29 ± 4.62	–
	FCN	7.43 ± 3.71	−0.86
	U-net	7.94 ± 3.50	−0.35
	MTLSegNet	$\mathbf{8.61} \pm \mathbf{4.27}$	0.32
CC-MLO ($n = \mathbf{6,840}$)	Radiologist	9.42 ± 5.38	–
	FCN	9.61 ± 4.68	0.19
	U-net	11.32 ± 6.16	1.9
	MTLSegNet	$\mathbf{9.42} \pm \mathbf{5.28}$	0

Table 5. Descriptive summary of estimated PD values by the FCN, U-net, and MTLSegNet approaches on the KUH evaluation dataset. We use the mean and the standard deviation (SD) to illustrate the distribution of the PD values and compare the robustness of the model predictions. The number in the brackets denotes the number of mammograms in each view of the KUH evaluation dataset. The last column represents the mean difference between the estimated PD values and the radiologist-provided PD values. We highlighted the model, whose mean difference is close to the reference (radiologist) mean PD value. Lower the mean difference, better the model performance. The negative mean difference indicates that the model has underestimated the PD values compared to the radiologist-provided PD values. Best values are in [bold].

KUH evaluation dataset ($n = 6840$)			
View	**PD estimation**	***r [95% CI]***	***p-value***
CC ($n = \mathbf{3,528}$)	FCN	0.88 [0.88, 0.89]	< 0.001
	U-net	0.87 [0.87, 0.88]	< 0.001
	MTLSegNet	**0.90 [0.90, 0.91]**	$< \mathbf{0.001}$
MLO ($n = \mathbf{3,312}$)	FCN	0.89 [0.89, 0.91]	< 0.001
	U-net	0.86 [0.86, 0.88]	< 0.001
	MTLSegNet	**0.91 [0.91, 0.92]**	$< \mathbf{0.001}$
CC-MLO ($n = \mathbf{6,840}$)	FCN	0.88 [0.89, 0.89]	< 0.001
	U-net	0.84 [0.83, 0.85]	< 0.001
	MTLSegNet	**0.90 [0.89, 0.91]**	$< \mathbf{0.001}$

Table 6. The Pearson correlation between the estimated PD values and radiologist-provided PD values at 95% confidence interval. For all three CC-, MLO-, and CC-MLO-view mammograms, MTLSegNet shows a higher correlation than the baseline models. Before correlation analysis, we applied a log transform to all density values. We highlighted the model with strongest correlation with the radiologist PD values. Best values are in [bold].

the radiologist assessment. The distribution of density values for the KUH evaluation set are left skewed. Appendix E shows the distribution of the estimated density values on the KUH evaluation dataset for all models.

Table 6 shows the Pearson correlation coefficient between the radiologist-provided PD and estimated PD from the FCN, U-net, and MTLSegNet models. MTLSegNet shows a higher correlation of $r = 0.90$ [95% CI 0.89, 0.91] (p value < 0.001) with the radiologist-provided PD values than the FCN and U-net models, with $r = 0.88$ (p value < 0.001) and $r = 0.84$ (p value < 0.001), respectively, for the CC-MLO-view mammograms. Additionally, we performed a statistical analysis within the DL approaches. For the CC-MLO-view of the KUH evaluation data, MTLSegNet-estimated PD values are significantly better than FCN and U-net with p values < 0.001. However, in the CC-view mammograms, FCN- and MTLSegNet-estimated PD values did not show significant difference (p value> 0.01).

LIBRA and quantra overestimate the breast-density values. Table 7 provides summary statistics of the estimated PD values by the LIBRA, Quantra, and MTLSegNet approaches on the KUH evaluation set for the CC-, MLO-, and CC-MLO-view mammograms. For the CC-MLO-view, the mean PD values estimated by Quantra, LIBRA, and MTLSegNet were $16.18 \pm 15.66, 14.33 \pm 11.85$, and 9.42 ± 5.28, respectively. For the CC-MLO-view mammograms, the mean PD differences between Quantra and LIBRA and the radiologist assessment were 6.76% and 4.91%, respectively, indicating that both Quantra and LIBRA overestimated the PD values (the mean PD

KUH evaluation set ($n = 6840$)			
View	**PD estimation**	**Mean ± SD**	**$PD_{model} - PD_{radiologist}$**
CC ($n = $ **3,528**)	Radiologist	10.38 ± 5.77	-
	MTLSegNet	**11.28 ± 5.75**	0.9
	LIBRA	14.89 ± 12.34	4.51
	Quantra	16.22 ± 15.53	5.84
MLO ($n = $ **3,312**)	Radiologist	8.29 ± 4.62	-
	MTLSegNet	**8.61 ± 4.27**	0.32
	LIBRA	13.66 ± 11.21	5.37
	Quantra	16.13 ± 15.82	7.84
CC-MLO ($n = $ **6,840**)	Radiologist	9.42 ± 5.38	-
	MTLSegNet	**9.42 ± 5.28**	0
	LIBRA	14.33 ± 11.85	4.91
	Quantra	16.18 ± 15.66	6.76

Table 7. Descriptive summary of estimated PD values of MTLSegNet, LIBRA, and Quantra and the radiologist-assessed PD values using the KUH evaluation set. We show the mean and standard deviation (SD) of the PD values for all models. We highlighted the model, whose mean difference is close to the reference (radiologist) mean PD value. Lower the mean difference, better the model performance. Best values are in [bold].

KUH evaluation set ($n = 6840$)			
View	**PD estimation**	***r [95% CI]***	***p-value***
CC ($n = 3528$)	Radiologist Vs MTLSegNet	**0.90 [0.90, 0.91]**	< 0.001
	Radiologist Vs LIBRA	0.66 [0.65, 0.68]	< 0.001
	Radiologist Vs Quantra	0.64 [0.63, 0.67]	< 0.001
MLO ($n = 3312$)	Radiologist Vs MTLSegNet	**0.91 [0.91, 0.92]**	< 0.001
	Radiologist Vs LIBRA	0.68 [0.66, 0.67]	< 0.001
	Radiologist Vs Quantra	0.64 [0.62, 0.67]	< 0.001
CC-MLO ($n = 6840$)	Radiologist Vs MTLSegNet	**0.90 [0.89, 0.91]**	< 0.001
	Radiologist Vs LIBRA	0.67 [0.66, 0.68]	< 0.001
	Radiologist Vs Quantra	0.64 [0.63, 0.65]	< 0.001

Table 8. The Pearson correlation computed between the radiologist-provided PD values and the estimated PD values from MTLSegNet, LIBRA, and Quantra at 95% CIs on the log-transformed PD values. The models with high correlation are highlighted. For both CC- and MLO-view mammograms, our proposed approach demonstrated a strong correlation with the radiologist-provided density values. Best values are in [bold].

value assessed by the radiologists was 9.42% for the CC-MLO-view images). Appendix F shows details of the distribution of the estimated density values on the KUH evaluation set for MTLSegNet, LIBRA, and Quantra. The maximum PD values estimated by LIBRA and Quantra were 62% and 86%, respectively, while the maximum reference PD value in the KUH evaluation set was 48%. In Appendix G, we show a qualitative visualization of the limitations of LIBRA segmentation and compared it with MTLSegNet to illustrate the success of our proposed approach in segmenting the breast area and the dense tissues for more accurate PD value estimation.

Table 8 provides the correlation of estimated PD values from the LIBRA, Quantra, and MTLSegNet approaches with the radiologist PD values. The PD estimated by MTLSegNet strongly correlates with the radiologist-provided PD values. For the CC-MLO-view images, the proposed MTLSegNet model shows a strong correlation of $r = 0.90$ [95% CI 0.89, 0.91] with p value < 0.001, while LIBRA and Quantra show high correlations of $r = 0.67$ [95% CI 0.66, 0.68] and $r = 0.64$ [95% CI 0.63, 0.65], respectively, with p values < 0.001. In Appendices F and G, we qualitatively demonstrate the breast and dense-tissue segmentations from LIBRA and compared them with the MTLSegNet approach. LIBRA failed to exclude the pectoral and abdominal tissues from the breast-area segmentation and over-segmented the dense tissues, resulting in an overestimate of the PD values. The Quantra software tool provides only the PD values; thus, we were not able to compare the intermediate visualizations of breast and dense-tissue segmentations. We report the correlation between LIBRA and the radiologist on an evaluation set of 6840 mammograms. The correlation results are in agreement with Lee and Nishikawa[14], who showed a Pearson correlation of $r = 0.69$ for the CC-MLO-view mammograms on an evaluation set of 91 mammograms. These results indicate that our proposed model more accurately estimates the breast density values than the existing LIBRA and Quantra tools.

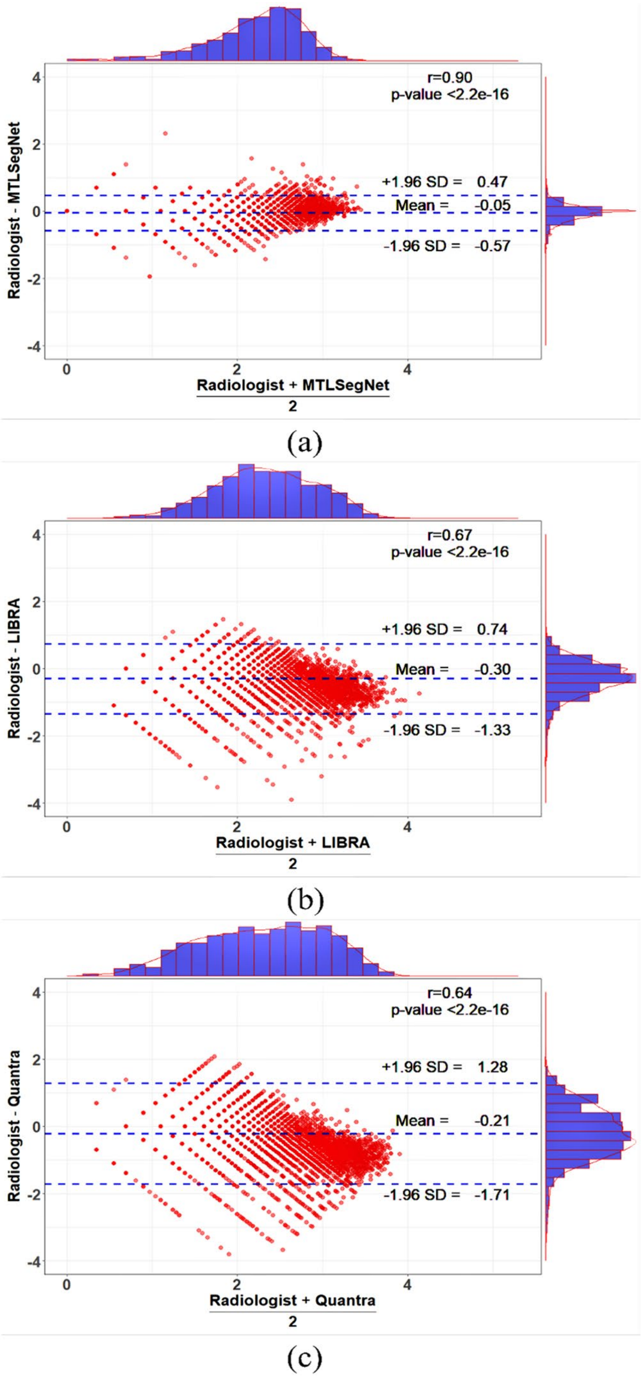

Figure 8. Bland–Altman agreement plots for MTLSegNet, LIBRA, and Quantra with the radiologist-provided PD values for the KUH evaluation dataset. The center blue dotted line shows the average PD values for the two methods. The dotted lines on the top and bottom indicate the LoA range, that is, the value at 1.96 times the standard deviation (SD) in both directions. If the data points are within the LoA, the two methods have strong agreement, otherwise the methods disagree. The Bland-Altman plots are shown for (**a**) MTLSegNet, (**b**) LIBRA, and (**c**) Quantra on the KUH evaluation dataset for the CC-MLO-view mammograms.

Additionally, Fig. 8 shows Bland–Altman agreement plots for MTLSegNet, LIBRA, and Quantra with the radiologist-provided PD values for the KUH evaluation dataset. The estimated PD values using the MTLSegNet approach show a strong agreement with the radiologist (98.6% CDI acceptance range) with LoA from −0.54 to 0.52 with a mean bias of −0.008 on the log-transformed scale. LIBRA and Quantra show moderate agreement with the radiologist with 82.75% and 80.87% CDI acceptance rates, respectively, and mean biases of −0.26 (LoA: −1.33 to 0.74) and −0.21 (LoA: −1.70 to 1.28).

Discussion

In this study, we developed a DL approach for estimating area-based breast PD value in mammograms using a weight-adaptive multitask learning approach based on 21,315 mammograms from KUH and 10,416 mammograms from the open-source datasets. The results showed that the proposed approach successfully segmented the breast area and the dense tissues and could estimate the breast density with higher precision than the existing LIBRA and Quantra tools. The main reasons for the outstanding performance of MTLSegNet are as follows. First, the model consisted of two task-specific decoders, with the dense-tissue segmentation, as the primary task, and the breast-area segmentation, as the auxiliary task. This architecture helped the model to exclude tissues or organs that adversely affected the segmentation and thus, estimation of the PD values; Second, the proposed model was trained end-to-end with a modified weight-adaptive multitask learning loss function, which enabled the network to generate more accurate predictions; and third, the model was trained using combination of all the training mammograms from all datasets. Datasets had different data distributions; therefore, the model learned from multi-vendor, multi-resolution, and multi-intensity variations, and preferably only a single model was generated for evaluation. Results in Table 4 showed that our model achieved excellent segmentation performance not only for each individual dataset, but also the combined evaluation set of all datasets. The proposed approach successfully segmented the breast area and the dense tissues more precisely than the multitask U-net and FCN approaches by on average, 3.17% and 2.29% relative improvements, in terms of F-score, respectively, in the combined CC-MLO-view data. The estimated PD values using our approach also showed a strong correlation with the values provided by the expert radiologists with a Pearson correlation $r = 0.90$ (p value < 0.001).

In our study, 6840 out of 7500 mammograms from the KUH evaluation set were within the CDI range and therefore, considered for evaluation. The assessed density values of the excluded 660 mammograms were not in agreement between the radiologists mainly due to the poor quality of the mammograms and blood vessels embedded within the dense tissues. We additionally correlated the PD values estimated by our model with values given by each radiologist for these 660 excluded mammograms. As expected, we obtained moderate correlations with $r = 0.715$ [95% CI 0.706, 0.721] and $r = 0.736$ [95% CI 0.725, 0.746] for such mammograms.

The training sizes of MIAS ($n = 194$) and INbreast ($n = 246$) datasets were considerably lower than KUH ($n = 11{,}052$) and mini-DDSM ($n = 5812$). Additionally, the resolution of mammograms and distribution of pixel intensities were different among the datasets (see Fig. 2). Therefore, the model, trained on the combined training sets of all datasets, has been biased towards datasets having larger training data, i.e., KUH and mini-DDSM. This partly explains that why F-score and IoU values for the MIAS and INbreast datasets were relatively lower compared to the KUH and mini-DDSM datasets in Table 4.

The density assessment in the BI-RADS classification subjects to the radiologist's experience and often shows intra- and inter-reader variability. Our data-driven DL approach for the density estimation is reproducible, scalable, and furthermore, provides density scores in a continuous percentage scale, which reduces the subjectivity. MTLSegNet accepts mammograms in DICOM format (or any other imaging format) irrespective of the acquisition manufacturer and device model, thus easily scalable. The inference time takes about a minute to estimate density values for 100 mammograms. Our method is, however, able to classify mammograms into BI-RADS density categories. We additionally performed a BI-RADS classification on the INbreast and mini-DDSM evaluation data, where BI-RADS density categories were available. The estimated PD values for these two datasets were categorized into 25% density intervals in line with the BI-RADS 4th edition categories, i.e., 0–25% (category 1), 26–50% (category 2), 51–75% (category 3), and 76–100% (category 4). Our proposed approach successfully classified the INbreast and mini-DDSM evaluation data into BI-RADS categories with accuracies of 87% and 92%, respectively, comparable to the results reported in[56,57].

Although our proposed approach improves the density estimation, it has a few limitations. The proposed model is restricted to the area-based density estimation. Moreover, due to the stochastic and non-linear nature of the DL methods, it is important to investigate the model uncertainty in predictions, which we leave it to a future study (Supplementary Information).

Conclusion

To conclude, we developed a reliable and scalable model to estimate area-based breast density from mammograms. The proposed approach showed consistent results and would assist the radiologist in personalized screening settings. In future study, we extend this model to volumetric breast-density estimation by incorporating the concepts of generative adversarial networks to generate the ground-truth segmentations more effectively. This will reduce the time consumed by manually creating the ground-truth segmentations. We will also investigate various uncertainty qualification techniques to improve the model performance and to build trust among radiologist to incorporate the DL algorithms in regular screening workflow. The estimated PD values will be incorporated into BC risk-prediction models in our future studies.

Data availability

The KUH imaging data and the corresponding annotations used in this study are available under request to the corresponding author. MIAS and mini-DDSM datasets are open source and publicly available. Annotations of these two datasets are provided in the manuscript GitLab page at https://gitlab.com/rajgudhe.uef/mtlsegnet. INbreast dataset is available with the data owner, contact inesdomingues@gmail.com for more details.

Code availability

All the implementation source codes, the annotation tool, and the trained models are open-source and freely available online in the manuscript GitLab page at https://gitlab.com/rajgudhe.uef/mtlsegnet. A representative website demo is also shown in Fig. 9. During mammogram upload, the data provider gives consent that the image

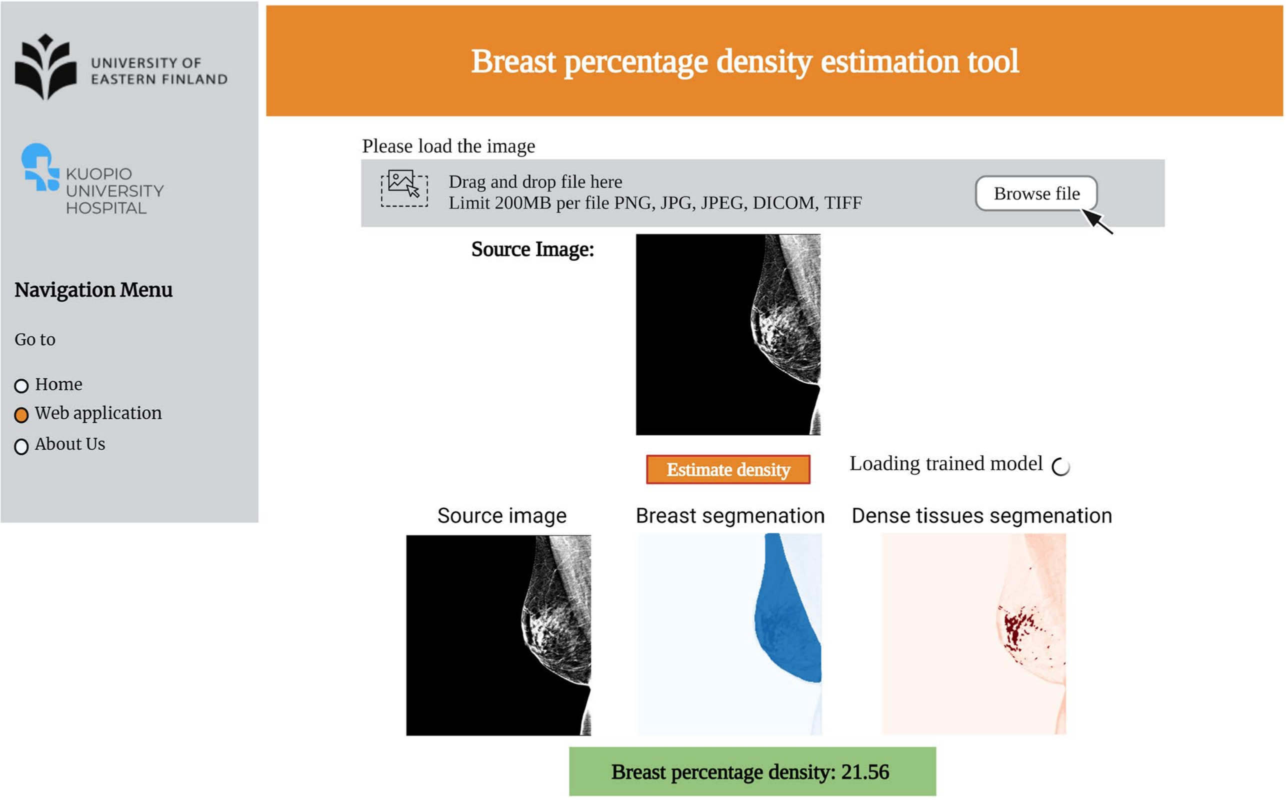

Breast percentage density: 21.56

Figure 9. Sample website report of the MTLSegNet PD estimation model.

is used for segmentation and density estimation. We expect this web platform will act as a hub for radiologists to efficiently assess the breast density so that inter- and intra-reader variability are considerably decreased.

Received: 23 March 2022; Accepted: 5 July 2022
Published online: 14 July 2022

References

1. Amendoeira, I. *et al. European Guidelines for Quality Assurance in Breast Cancer Screening and Diagnosis*. 1–160 (2013).
2. McCormack, V. A. & dos Santos Silva, I. Breast density and parenchymal patterns as markers of breast cancer risk: A meta-analysis. *Cancer Epidemiol. Prev. Biomark.* **15**, 1159–1169 (2006).
3. Vachon, C. M. *et al.* Mammographic density, breast cancer risk and risk prediction. *Breast Cancer Res.* **9**, 1–9 (2007).
4. Vachon, C. M., Kuni, C. C., Anderson, K., Anderson, V. E. & Sellers, T. A. Association of mammographically defined percent breast density with epidemiologic risk factors for breast cancer (united states). *Cancer Causes Control* **11**, 653–662 (2000).
5. Holland, K., van Gils, C. H., Mann, R. M. & Karssemeijer, N. Quantification of masking risk in screening mammography with volumetric breast density maps. *Breast Cancer Res. Treat.* **162**, 541–548 (2017).
6. von Euler-Chelpin, M., Lillholm, M., Vejborg, I., Nielsen, M. & Lynge, E. Sensitivity of screening mammography by density and texture: A cohort study from a population-based screening program in denmark. *Breast Cancer Res.* **21**, 1–7 (2019).
7. Sickles, E. *et al.* Breast imaging reporting and data systems. *ACR BI-RADS Atlas Breast Imaging Rep. Data Syst.* **5**, 25 (2013).
8. Destounis, S. *et al.* Using volumetric breast density to quantify the potential masking risk of mammographic density. *Am. J. Roentgenol.* **208**, 222–227 (2017).
9. Alikhassi, A., Gourabi, H. E. & Baikpour, M. Comparison of inter-and intra-observer variability of breast density assessments using the fourth and fifth editions of Breast Imaging Reporting and Data System. *Eur. J. Radiol. Open* **5**, 67–72 (2018).
10. Byng, J. W., Boyd, N., Fishell, E., Jong, R. & Yaffe, M. J. The quantitative analysis of mammographic densities. *Phys. Med. Biol.* **39**, 1629–1638 (1994).
11. Gomez, I. M., El Busto, M. C., Guirao, J. A., Perales, F. R. & Azpitarte, R. L. Semiautomatic estimation of breast density with DM-Scan software. *Radiology (English Ed.)* **56**, 429–434 (2014).
12. Keller, B. M. *et al.* Estimation of breast percent density in raw and processed full field digital mammography images via adaptive fuzzy c-means clustering and support vector machine segmentation. *Med. Phys.* **39**, 4903–4917 (2012).
13. Hartman, K., Highnam, R., Warren, R. & Jackson, V. Volumetric assessment of breast tissue composition from FFDM images. In *International Workshop on Digital Mammography*, 33–39 (2008).
14. Lee, J. & Nishikawa, R. M. Automated mammographic breast density estimation using a fully convolutional network. *Med. Phys.* **45**, 1178–1190 (2018).
15. Zanaty, E. & Ghoniemy, S. Medical image segmentation techniques: An overview. *Int. J. Inform. Med. Data Process.* **1**, 16–37 (2016).
16. Chen, C. W., Luo, J. & Parker, K. J. Image segmentation via adaptive k-mean clustering and knowledge-based morphological operations with biomedical applications. *IEEE Trans. Image Process.* **7**, 1673–1683 (1998).
17. Van Grinsven, Mark JJP., van Ginneken, B., Hoyng, C. B., Theelen, T. & Sánchez, C. I. Fast convolutional neural network training using selective data sampling: Application to hemorrhage detection in color fundus images. *IEEE Trans. Med. Imaging* **35**, 1273–1284 (2016).
18. Esteva, A. *et al.* Dermatologist-level classification of skin cancer with deep neural networks. *Nature* **542**, 115–118 (2017).

19. Ronneberger, O., Fischer, P. & Brox, T. U-net: Convolutional networks for biomedical image segmentation. In *International Conference on Medical Image Computing and Computer-Assisted Intervention*, 20:234–241 (2015).
20. Long, J., Shelhamer, E. & Darrell, T. Fully convolutional networks for semantic segmentation. In *Proceedings of the IEEE Conference on Computer Vision and Pattern Recognition*, 3431–3440 (2015).
21. Amer, A., Ye, X., Zolgharni, M. & Janan, F. ResDUnet: Residual Dilated UNet for Left Ventricle Segmentation from Echocardiographic Images. 2019–2022 (2020).
22. Gudhe, N. R. *et al.* Multi-level dilated residual network for biomedical image segmentation. *Sci. Rep.* **11**, 14105–14105 (2021).
23. Kendall, A., Gal, Y. & Cipolla, R. Multi-task learning using uncertainty to weigh losses for scene geometry and semantics. In *Proceedings of the IEEE Conference on Computer Vision and Pattern Recognition*, 7482–7491 (2018).
24. Caruana, R. Multitask learning. *Mach. Learn.* **28**, 41–75 (1997).
25. Ruder, S. An overview of multi-task learning in deep neural networks. arXiv:1706.05098 (arXiv preprint) (2017).
26. Lehman, C. D. *et al.* Mammographic breast density assessment using deep learning: Clinical implementation. *Radiology* **290**, 52–58 (2019).
27. Li, S. *et al.* Computer-aided assessment of breast density: Comparison of supervised deep learning and feature-based statistical learning. *Phys. Med. Biol.* **63**, 14 (2018).
28. Ahn, C. K., Heo, C., Jin, H. & Kim, J. H. A novel deep learning-based approach to high accuracy breast density estimation in digital mammography. In *Medical Imaging 2017: Computer-Aided Diagnosis*, 10134 (2017).
29. Fonseca, P. et al. Automatic breast density classification using a convolutional neural network architecture search procedure. In *Medical Imaging 2015: Computer-Aided Diagnosis* 9414 (2015).
30. Kallenberg, M. *et al.* Unsupervised deep learning applied to breast density segmentation and mammographic risk scoring. *IEEE Trans. Med. Imaging* **35**, 1322–1331 (2016).
31. Gemici, A. A., Bayram, E., Hocaoglu, E. & Inci, E. Comparison of breast density assessments according to BI-RADS 4th and 5th editions and experience level. *Acta Radiol. Open* **9**, 25 (2020).
32. Wirth, M. A. & Stapinski, A. Segmentation of the breast region in mammograms using active contours. *Visual Commun. Image Process.* **5150**, 1995–2006 (2003).
33. Rampun, A., Morrow, P. J., Scotney, B. W. & Winder, J. Fully automated breast boundary and pectoral muscle segmentation in mammograms. *Artif. Intell. Med.* **79**, 28–41 (2017).
34. Suckling, J. P. The mammographic image analysis society digital mammogram database exerpta medica. *Digit. Mammo* **1069**, 375–378 (1994).
35. Lekamlage, C. D., Afzal, F., Westerberg, E. & Cheddad, A. Mini-DDSM: Mammography-based automatic age estimation. In *International Conference on Digital Medicine and Image Processing*, 1–6 (2020).
36. Moreira, I. C. *et al.* INbreast: Toward a full-field digital mammographic database. *Acad. Radiol.* **19**, 236–248 (2012).
37. Rose, C., Turi, D., Williams, A., Wolstencroft, K. & Taylor, C. Web services for the DDSM and digital mammography research. In *International Workshop on Digital Mammography*, 376–383 (2006).
38. StandardScaler. Accessed on 25.02.2022.
39. Wirth, M. A. & Stapinski, A. Segmentation of the breast region in mammograms using active contours. *Int. Soc. Opt. Photon.* **5150**, 1995–2006 (2003).
40. Dutta, A. & Zisserman, A. The VIA annotation software for images, audio and video. *Proc. Int. Conf. Multimed.* **4**, 2276–2279 (2019).
41. Chen, L.-C., Papandreou, G., Kokkinos, I., Murphy, K. & Yuille, A. L. Deeplab: Semantic image segmentation with deep convolutional nets, atrous convolution, and fully connected crfs. *IEEE Trans. Pattern Anal. Mach. Intell.* **40**, 834–848 (2017).
42. Sharma, S., Sharma, S. & Athaiya, A. Activation functions in neural networks. *Towards Data Sci.* **6**, 310–316 (2017).
43. Abraham, N. & Khan, N. M. A novel focal tversky loss function with improved attention u-net for lesion segmentation. In *International Symposium on Biomedical Imaging*, 683–687 (2019).
44. Kendall, A. & Gal, Y. What uncertainties do we need in bayesian deep learning for computer vision? Computing Research Repository. arXiv:1703.04977 (2017).
45. Paszke, A. *et al.* Pytorch: An imperative style, high-performance deep learning library. *Adv. Neural Inf. Process. Syst.* **32**, 25 (2019).
46. Xu, X., Xu, S., Jin, L. & Song, E. Characteristic analysis of otsu threshold and its applications. *Pattern Recogn. Lett.* **32**, 956–961 (2011).
47. Balandat, M. *et al.* BoTorch: A framework for efficient Monte-Carlo Bayesian optimization. *Adv. Neural. Inf. Process. Syst.* **33**, 21524–21538 (2020).
48. Adaptive Experimentation Platform. Accessed on 25.02.2022.
49. Ioffe, S. & Szegedy, C. Batch normalization: Accelerating deep network training by reducing internal covariate shift. In *International Conference on Machine Learning*, 448–456 (2015).
50. Ulyanov, D., Vedaldi, A. & Lempitsky, V. S. Instance normalization: The missing ingredient for fast stylization. Computing Research Repository. arXiv:1607.08022 (2016).
51. Wu, Y. & He, K. Group normalization. *Int. J. Comput. Vis.* **128**, 742–755 (2020).
52. Qiao, S., Wang, H., Liu, C., Shen, W. & Yuille, A. L. Weight standardization. Computing Research Repository. arXiv:1903.10520 (2019).
53. IT Service Centre for Science (CSC) . Accessed on 25.02.2022.
54. Pearson, K. VII. Mathematical contributions to the theory of evolution-III. Regression, heredity, and panmixia. *Philos. Trans. R. Soc. Lond. Ser. A* **20**, 253–318 (1896).
55. Giavarina, D. Understanding bland Altman analysis. *Biochem. Med.* **25**, 141–151 (2015).
56. Falconí, L., Pérez, M., Aguilar, W. & Conci, A. Transfer learning and fine tuning in mammogram bi-rads classification. In *2020 IEEE 33rd International Symposium on Computer-Based Medical Systems (CBMS)*, 475–480 (IEEE, 2020).
57. Medeiros, A., Ohata, E. F., Silva, F. H., Rego, P. A. & Reboucas Filho, P. P. An approach to bi-rads uncertainty levels classification via deep learning with transfer learning technique. In *2020 IEEE 33rd International Symposium on Computer-Based Medical Systems (CBMS)*, 603–608 (IEEE, 2020).

Acknowledgements

This study is supported by Grants from the European regional development fund and the Cancer Society of Finland.

Author contributions

N.R.G. involved in conceptualization, methodology, software, and writing the original draft. H.B. involved in conceptualization, methodology, validation, writing, review, and editing. M.S., H.O., R.V., V.-M.K., and A.M. involved in conceptualization, writing, review, and editing.

Competing interests

The authors declare no competing interests.

Additional information

Supplementary Information The online version contains supplementary material available at https://doi.org/10.1038/s41598-022-16141-2.

Correspondence and requests for materials should be addressed to N.R.G. or H.B.

Reprints and permissions information is available at www.nature.com/reprints.